Size-effects affecting the fatigue response up to 109 cycles (VHCF) of SLM AlSi10Mg specimens produced in horizontal and vertical directions

Original
Size-effects affecting the fatigue response up to 109 cycles (VHCF) of SLM AlSi10Mg specimens produced in horizontal and vertical directions / Tridello, A., Fiocchi, J., Biffi, C.A., Rossetto, M., Tuissi, A., Paolino, D.S.. - In: INTERNATIONAL JOURNAL OF FATIGUE. - ISSN 0142-1123. - 160:(2022), p. 106825. [10.1016/j.ijfatigue.2022.106825]

Publisher:
ELSEVIER SCI LTD

Published
DOI:10.1016/j.ijfatigue.2022.106825

Size-effects affecting the fatigue response up to 10^9 cycles (VHCF) of SLM AlSi10Mg specimens produced in horizontal and vertical directions

Authors:
A. Tridello[a], J. Fiocchi[b], C.A. Biffi[c], M. Rossetto[d], A. Tuissi[e], D.S. Paolino[f]

[a] Department of Mechanical and Aerospace Engineering, Politecnico di Torino, 10129 Turin, Italy, andrea.tridello@polito.it
[b] CNR ICMATE – Institute of Condensed Matter Chemistry and Technologies for Energy, 23900 Lecco, Italy, jacopo.fiocchi@icmate.cnr.it
[c] CNR ICMATE – Institute of Condensed Matter Chemistry and Technologies for Energy, 23900 Lecco, Italy, carloalberto.biffi@cnr.it
[d] Department of Mechanical and Aerospace Engineering, Politecnico di Torino, 10129 Turin, Italy, massimo.rossetto@polito.it
[e] CNR ICMATE – Institute of Condensed Matter Chemistry and Technologies for Energy, 23900 Lecco, Italy, ausonio.tuissi@cnr.it
[e] Department of Mechanical and Aerospace Engineering, Politecnico di Torino, 10129 Turin, Italy, davide.paolino@polito.it

Corresponding Author:
A. Tridello
E-mail address: andrea.tridello@polito.it
Full postal address:
C.so Duca degli Abruzzi 24,
Department of Mechanical and Aerospace Engineering – Politecnico di Torino,
10129 – Turin,
ITALY
Phone number: +39.011.090.6913
Fax number: +39.011.090.6999

Abstract

This paper experimentally investigates the effect of the specimen volume (size-effect) on the Very-High-Cycle-Fatigue (VHCF) response of SLM AlSi10Mg specimens. Tension-compression tests are carried out on hourglass and Gaussian specimens with different risk-volumes produced in horizontal and vertical direction. Experimental results show that size-effects significantly influence the VHCF response regardless of the building orientation. Furthermore, size-effects are more evident for SLM specimens than for traditionally built specimens, pointing out that the design of SLM components cannot rely on the results obtained by testing traditionally built specimens.

Keywords: VHCF; Additive Manufacturing (AM); Selective Laser Melting (SLM); Aluminium alloy; size-effect.

1. INTRODUCTION

In the last years, components manufactured through Additive Manufacturing (AM) technologies have been used in a growing number of industrial applications [1, 2]. The efforts of academic and industrial researchers are currently focused on the development of safe design methodologies [3, 4] for AM components to guarantee their Structural Integrity (SI, [5, 6]). Indeed, due to the additive process, the microstructure and the resulting mechanical properties of AM parts are intrinsically different from those of traditionally built (TB) components [7] (e.g., obtained through casting or subtractive processes, like machining). For applications in which quasi-static loads are involved, components are generally designed (or redesigned) through topology optimization algorithms [8, 9]. During the optimization process, the allowable stresses are the yield strength or the tensile strength of the material, which are generally close or better than those of TB parts [5], mainly due to the fine microstructure resulting from the AM process [10-12]. Moreover, the limited ductility of as-built AM parts can be properly controlled through traditional or specific heat treatments or through an optimization of the process parameters [13]. For these reasons, brackets [14], heat exchanger [15] or biomedical implants [16], can be reliably designed by considering the maximum applied static load and safely employed.

On the other hand, the SI of components subjected to fatigue loads is still an issue [17-19]. The main criticality associated with the worse fatigue behaviour of AM parts, if compared to that of TB parts, is the formation of large defects within the material during the manufacturing process [20]. The stress distribution is locally modified due to the presence of manufacturing defects and a local stress concentration arises, fostering the crack nucleation process and originating premature fatigue failures. Therefore, for a conservative design of AM components subjected to fatigue loads the size of the defect in the component volume should be known or reliably estimated. To this aim, the X-ray microcomputed tomography (microCT) technique can be exploited for a non-destructive assessment of the most critical defect [21, 22] and, consequently, for the estimation of the fatigue response. However, this technique is very expensive and time-consuming and can be applied only if the component has been already produced, not permitting design modifications or reviews. An alternative faster and cheaper method considers the defects originating the fatigue failure in small specimens during laboratory tests. In this second case, size-effect must be carefully taken into account, since the decrement of the fatigue response with the size or the material volume, in High Cycle Fatigue (HCF) [23] as well as in Very High Cycle Fatigue (VHCF) [24, 25], can be relevant. Generally, size-effect is experimentally verified by testing specimens with different size [24, 25] and the fatigue response for larger parts is statistically predicted. Despite its important implications on the SI of components to be designed, size-effects on the fatigue response of AM components have been rarely investigated in the literature, especially if the VHCF response is considered.

The experimental activity in the present paper aims at assessing size-effects on the response at very high number of cycles, VHCF, of AlSi10Mg specimens produced through the Selective Laser Melting (SLM) process. Ultrasonic fully reversed tension-compression fatigue tests up to 10^9 cycles have been carried out on Gaussian specimens [26] with large risk-volumes and on hourglass specimens built in horizontal and in vertical directions. Fracture surfaces have been observed with the Scanning Electron Microscope in order to investigate the failure origin. Size-effect has been statistically assessed by comparing the defect size, the P-S-N curves and the VHCF strength at 10^9 cycles for horizontally built and vertically built specimens in order to investigate the influence of the building direction. Finally, the VHCF strength decrement due to size-effects in SLM specimens has been compared with the decrement found for TB specimens [25], in order to discuss the differences and the implications on the design of AM parts.

2. MATERIALS AND METHODS

In this Section details on the SLM process, on the geometry of the specimens used for the assessment of size-effects and on the fatigue tests are reported.

2.1. SLM of AlSi10Mg specimens: powder and process parameters

The specimens used for the fatigue tests were produced with an SLM Solutions 500 HL quad 4x400W system by setting standard industrial process parameters. AlSi10Mg powder, produced through an atomization process, was characterized by an average size of $45\ \mu\mathrm{m}$ and 80% of particles lying in the $[20;\ 63]\ \mu\mathrm{m}$ range. The specimens were built with their main axis lying both parallel to the building direction (vertical samples) and perpendicular to it (horizontal samples) in order to assess also the influence of the building orientation. A combined contour – meander scanning strategy was used: as a consequence, the outer layer of samples, approximately $400\ \mu\mathrm{m}$ thick, was built with a different orientation with respect to the inner portion. The reduced section of horizontal samples was sustained by suitable supports. The process parameters and the powder chemical composition are summarized in Table 1.

Table 1: Specimen production: AlSi10Mg chemical composition and SLM parameters meters

AlSi10Mg powder							
Si	**Mg**	**Cu**	**Ni**	**Fe**	**Mn**	**Ti**	**Al**
10	0.4	< 0.25	< 0.05	< 0.25	< 0.1	0.15	bal
SLM parameters							
Power	*Platform temperature*	*Scan speed*	*Spot size*	*Hatch distance*	*Layer thickness*		
$350\ \mathrm{W}$	$150°\ \mathrm{C}$	$1.15\ \mathrm{m/s}$	$80\ \mu\mathrm{m}$	$170\ \mu\mathrm{m}$	$50\ \mu\mathrm{m}$		

For the quasi-static tests, standard dog-bone specimens, produced in horizontal and in vertical direction, were used [27, 28]. For the ultrasonic fatigue tests, two specimen geometries with different risk-volumes, hourglass and Gaussian, were tested. The risk-volume, V_{risk}, corresponds to the material region with a stress amplitude large enough to originate a fatigue crack if a critical defect is present. According to the literature [23, 24], almost all the fatigue failures originate in the material region characterized by a stress amplitude larger than the 90% of the maximum applied stress, V_{90}. Accordingly, the risk-volume is assumed as the V_{90} (i.e., $V_{risk} = V_{90}$), in the following. Standard hourglass specimens with a $V_{90} = 250\ \mathrm{mm}^3$ were designed according to [26, 29]. Gaussian specimens, whose gage length has a profile described by a Gaussian function, were used for increasing the V_{90} up to $2330\ \mathrm{mm}^3$. Indeed, the Gaussian profile ensures a uniform stress distribution along the gage length and permits to increase the tested V_{90}. A similar V_{90} increment is prevented in standard dog bone specimens due to a non-uniform stress distribution within the gage length [30]. The geometries of the tested hourglass and Gaussian specimens are shown in Figure 1a and 1b, respectively.

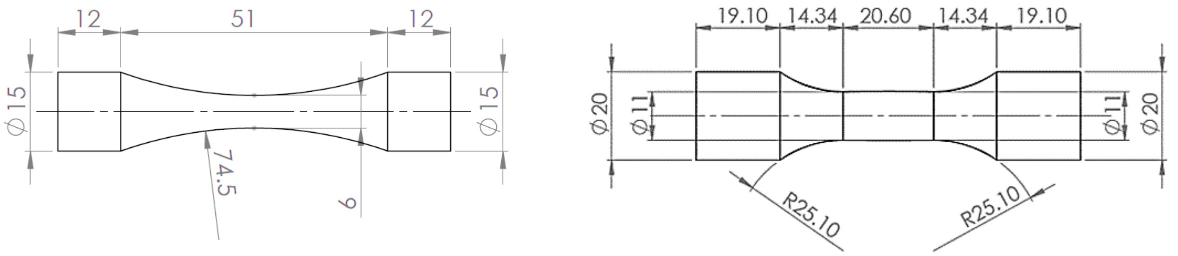

(a) (b)

Figure 1: Geometry of the tested specimens (not is scale, dimension in mm): a) hourglass specimen; b) Gaussian specimen.

For the design of the specimens, the dynamic elastic modulus, E_d, was measured through the Impulse Excitation Technique (IET, [31]). The E_d was similar and not dependent on the building orientation (i.e., the difference was small): therefore, the geometry of the specimens was the same, regardless of the building orientation. Support structures along the specimen length were used for manufacturing the horizontally built specimens. No heat treatment was applied after the production of the specimens, which were mechanically removed from the building platform.

The specimens were tested after a mechanical manual polishing. In particular, the specimens were gripped with a spindle, put in rotation and thereafter manually polished with sandpapers with increasing grit (from #120 to 1200#). Indeed, with the mechanical polishing a thin layer of material, averagely smaller than 0.2 mm is removed. In addition, the allowance required for polishing is smaller than that required if the specimens are machined (i.e., in the range $[0.5{:}1] \text{ mm}$, according to [32, 33]). Therefore, a smaller layer of material is removed from the surface, thus permitting to more properly assess the influence of surface and subsurface defects, together with internal defects. This procedure, commonly followed before VHCF tests [27, 34, 35], permits moreover to avoid premature failures due to large surface scratches and to assess the influence of surface and subsurface defects, which would be removed with other processes (e.g., machining of the specimens after the AM process). The surface roughness R_a of the tested specimens before and after the polishing process was measured on five specimens by using a *Mitutoyo Surftest SV-500* instrument. The average roughness before the polishing process was equal to 6.2 µm for the horizontally built specimens and equal to 5.7 µm for the vertically built specimens. After the polishing process, the average surface roughness Ra reduces to 1.4 µm for both specimen types.

2.2. Quasi-static and fatigue tests up to 10^9 cycles

Preliminary quasi-static tests were at first carried out to validate the process parameters. In particular, tensile tests on dog-bone specimens were carried out with a standard tensile testing machine (electromechanic MTS 2/M machine), following the ASTM E8/E8M-09 standard. The strain rate of the tests was equal to 0.015 mm^{-1} and the strain was measured with an extensometer. The Vickers hardness, HV, was also measured on the cross-section of the hourglass and Gaussian specimens, according to [27].

The ultrasonic fatigue testing machines (UFTMs) developed at the Politecnico di Torino were used for the ultrasonic (loading frequency of $20\ \mathrm{kHz}$) VHCF tests. Fully reversed tension-compression tests were carried out up to 10^9 cycles. The stress amplitude within the risk-volume was kept at the desired value with a feedback signal corresponding to the displacement amplitude measured at the free specimen end or to the strain amplitude measured by a strain gage attached to the horn. The applied stress amplitude was verified through a strain gage calibration.

The specimen temperature [36] was also continuously detected during the tests with an infrared pyrometer and kept below 25°C by cooling the specimens with two vortex tubes. Fig. 2 shows the UFTM testing machines used for the experimental tests on hourglass and on Gaussian specimens.

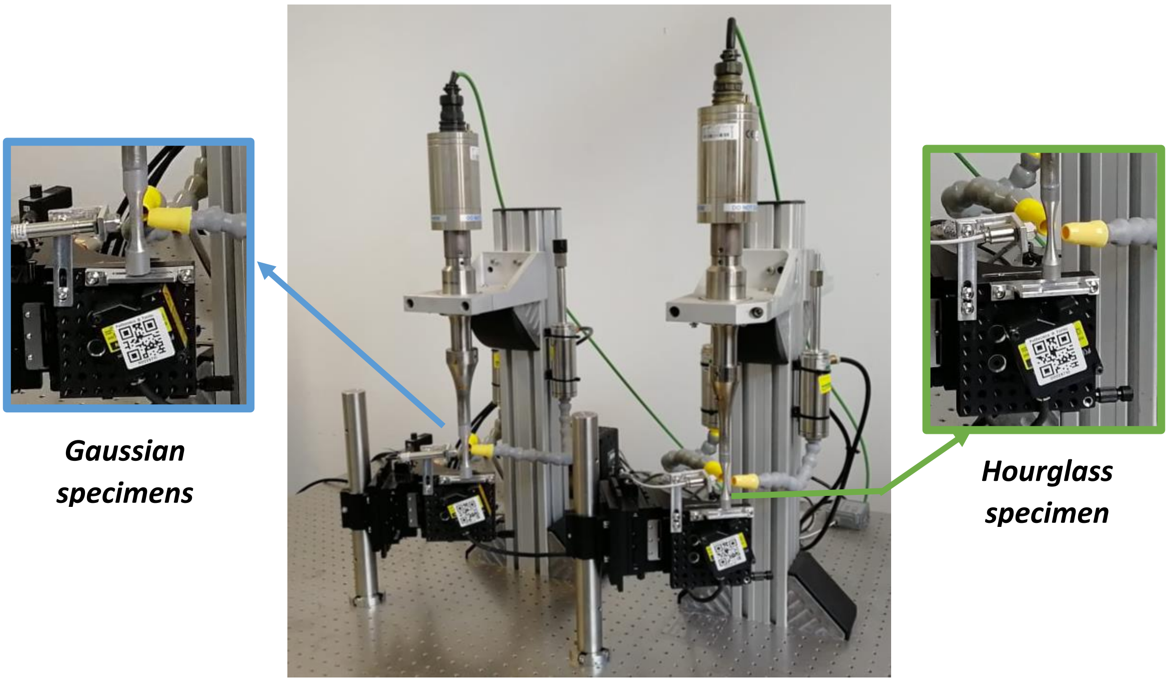

Figure 2: UFT machines used for testing the hourglass and the Gaussian specimens.

3. EXPERIMENTAL RESULTS

In this Section, the experimental results are statistically analysed and discussed, focusing on the effect of the specimen size and the building direction on the VHCF response.

In the following, HH and HV refer to the hourglass specimens horizontally and vertically built, respectively; whereas GH and GV refer to the Gaussians specimens horizontally and vertically built, respectively.

3.1. Microstructure, tensile properties and Vickers hardness

Preliminary microstructural analyses were at first carried out with the SEM. For both the horizontally and vertically built specimens, the microstructure was characterized by overlayed melt pools, which appear as semicircles in a polished section parallel to the building direction (Figure 3a) and as elongated stripes in the section parallel to the building plate (Figure 3b). At higher magnification (Figure 3c), the microstructure was characterized by an interconnected Si network dispersed within the supersaturated Aluminum α matrix. This microstructure is typical of as-built specimens [37]. For more details on the analysis of the microstructure the reader can refer to [28, 38]..

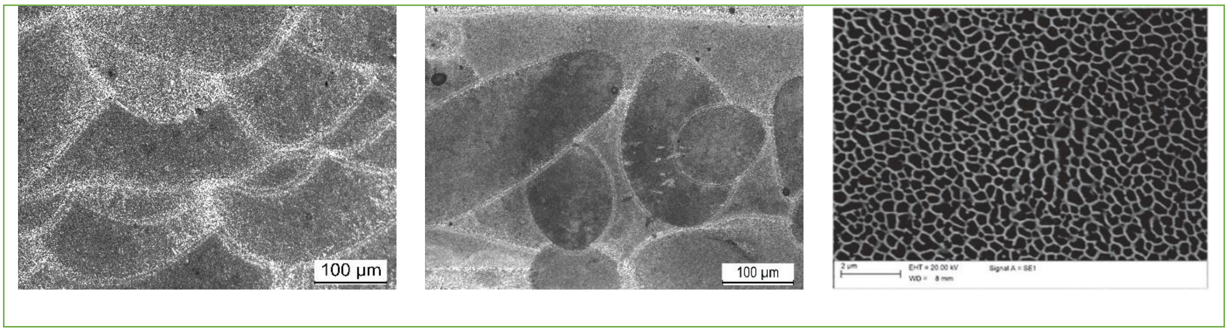

Figure 3: Representative microstructure of the tested AlSi10Mg specimens.

The quasi-static mechanical properties are thereafter analyzed. The yield strength σ_y, the ultimate tensile strength σ_u and the elongation to failure ε_f were assessed through a tensile test. The results are summarized in Table 2, together with the measured Vickers hardness. For the horizontally built specimens, the Vickers hardness reported within the two round brackets is the Vickers Hardness close to the material area where support structures were removed.

Table 2: tensile properties and Vickers hardness of the tested horizontal and vertical hourglass and Gaussian specimens.

Tensile properties			
	σ_y [MPa]	σ_u [MPa]	ε_f [%]
Horizontal	287 ± 5	413 ± 7	5.5 ± 0.1
Vertical	271 ± 4	419 ± 8	4.1 ± 0.1

Hardness				
Specimen type	***HH***	***GH***	***HV***	***GV***
Hardness [HV]	128 ± 1.5 (122)	134 ± 4 (121)	125 ± 1.7	146 ± 4

The mechanical properties obtained through quasi-static tensile tests, σ_y, σ_u and ε_f, on horizontal and vertical specimens were found to be close to those reported in the literature [39] and are analyzed and discussed in detail in [27, 28]. It is worth noting that the analysis of the tensile properties permits to validate the process parameters. According to the literature [40 Mower, 41 Bagherifard], tensile properties are generally experimentally measured with dog-bone specimens, as in the present paper, and are not expected to vary depending on the specimen type.

More attention was dedicated to the analysis of the Vickers hardness, correlated to the microstructure, according to [23]. The Vickers hardness of the Gaussian specimens was measured in [27] for the horizontally built specimens and in [28] for the specimens built in vertical direction. For the horizontally built specimens, the average value within the cross-section is very similar, with a difference smaller than 6 HV, whereas the HV is slightly smaller close to the support region for both the hourglass and the Gaussian specimens, being about 121 HV. This reduction may be justified by considering the microstructure emerging close to the support region, which coincides with the downskin area of the sample. Figure 4 clearly shows that a 200 μm thick layer exists at the very bottom of horizontally built samples: with respect to the bulk of SLMed parts, such layer is characterized by a coarser microstructure, which arises from the lower cooling rate locally caused by the presence of the underlying non-solidified powder. Indeed the eutectic Al-Si structure presents features which are intermediate between the cellular and dendritic domains of solidification mode. Moreover, numerous pores are concentrated inside this layer, presumably because of the local energy concentration induced by the insulating effect of underlying non solidified powder. Similar characteristics were found in the supported areas of SLMed steel parts too, as reported in [42]. On top of this transitional layer, the typical SLMed microstructure emerges, giving rise to the well-known alternation of fine and coarse areas inside semicircular melt pools. For vertically built specimens such variation in microstructure and, consequently, hardness was not revealed, but the difference between the Vickers hardness of hourglass and Gaussian specimens is larger: indeed, it reduces from $146\ \mathrm{HV}$ to $125\ \mathrm{HV}$. Since the same process parameters were considered when the specimens were manufactured, the difference could be due to the process variability and, probably, to local heat accumulation in thinner samples, as discussed in [43].

.

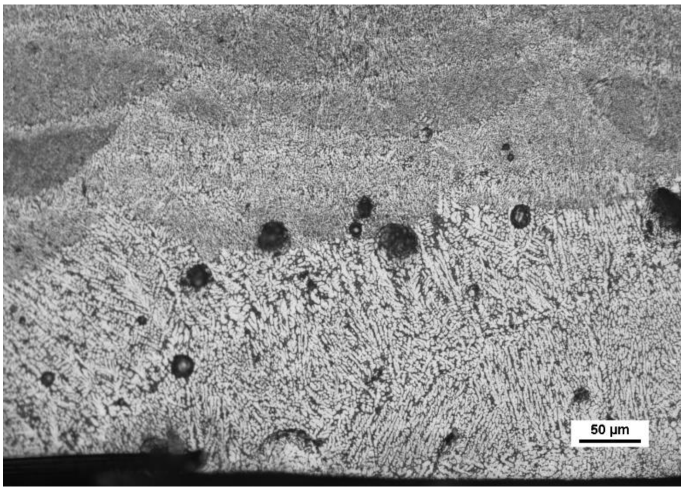

Figure 4: optical micrograph depicting the microstructure in the support region of GH and HH samples.

3.2. VHCF tests: S-N plot

Fig. 5 shows the S-N plot of the experimental data. All the fatigue failures originated from defects randomly distributed within the risk-volume. As for [25-28], the local stress, s_{local}, close to the defect originating the fatigue failure was considered in place of the stress at the specimen center.

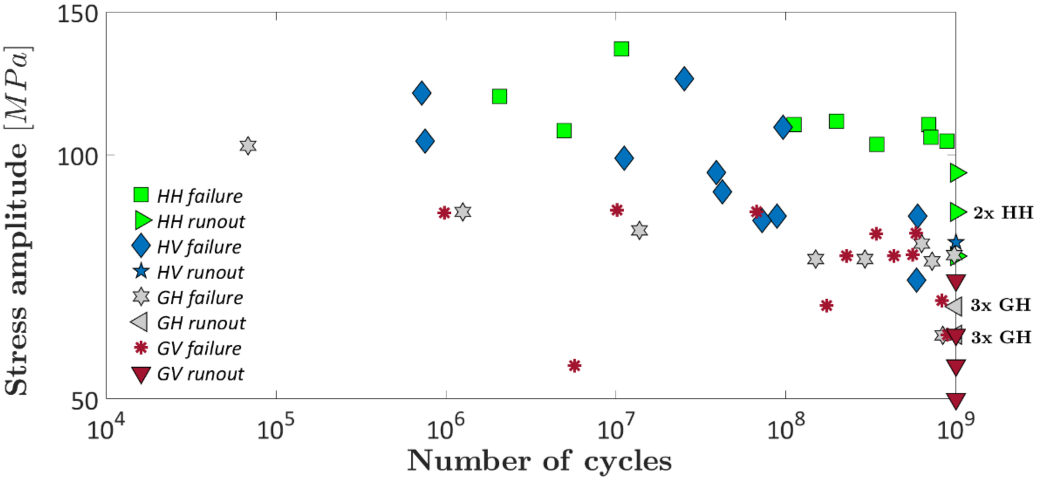

Figure 5: Experimental tests on HH, GH, HV and GV specimens: S-N plot.

According to Fig. 5, the experimental data are characterized by a large scatter, mainly associated with the scatter of the defect size. However, the influence of the specimen volume is visible by analyzing experimental failures and the experimental runouts. Indeed, for the same number of cycles to failure, N_f, the experimental failures occurred at larger stress amplitudes for the hourglass specimens with small V_{90}. The same trend can be seen by comparing the stress amplitude associated with the runout specimens. The experimental data for the vertically built specimens show in, general, a larger scatter, both in the hourglass and Gaussian specimens.

3.3 Defect analysis: location, type, and size

In order to properly compare the VHCF response of hourglass and Gaussian specimens, the defects at the origin of the VHCF failures (*critical defects* in the following) were analyzed with the SEM. It is worth noting that, in this analysis, only defects originating the fatigue failure, i.e., those controlling the fatigue response, have been considered. Indeed, even if other types of defects are present within the material volume, they have no effect on the VHCF response. For this reason, since the aim of the present work is to investigate size-effect on the critical defect size and, accordingly on the VHCF response, an analysis of the material defectiveness or a defect sampling was not considered, since it is out of the scope of the present work. Moreover, for defect rating, other inspection techniques, like the micro-CT, would be more appropriate.

The defect location within the cross-section was at first taken into consideration. Fig. 6 shows the radial distance from the specimen free surface of the critical defects. The radial distance has been computed as the minimum distance between the specimen free surface and the edge of the defect closest to the surface. According to [23], this distance permits to discriminate if a defect is a surface or an internal defect from the fracture mechanics point of view.

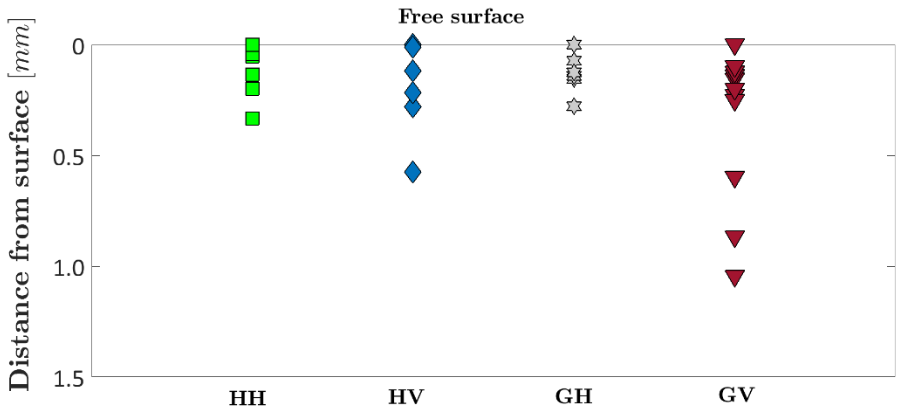

Figure 6: Radial distance from the specimen free surface of the critical defects in HH, HV, GH and GV specimens.

According to Fig. 6, almost all the defects are concentrated close to the free surface. For HH and GH specimens, all the defects are concentrated in a region of material with a maximum distance from the surface smaller than 500 μm. In particular, they are mainly close to the area where the support structures are removed, which is the weakest region within the cross-section. On the other hand, for vertically built specimens deeper critical defects were also found, with the 83% of the critical defects close to the surface (distance smaller than $500\ \mu\mathrm{m}$) and about the 17% of the critical defects at a distance from the surface in the range $[0.5 - 1.5]\ \mathrm{mm}$. In particular, critical defects are more dispersed for GV specimens, characterized by a cross-section with almost uniform microstructure and no weak regions.

Thereafter, the defect type was investigated (Fig. 7). Four types of critical defects, according to the classification provided in [44], were found: pores (Fig. 7a), defects due to improper layer bonding (ILB defect, Figure 7b), defects due to incomplete fusion (IC, Fig. 7c) and irregular surface defects (irregular SD, Fig. 7d). Incomplete fusion defects and defects due to improper layer bonding show similar morphology and appearance, even if their origin is different. Indeed, according to Fig. 7c, unmelted powder particles are generally visible in incomplete fusion defects, whereas a "stacked" appearance, without any unmelted material, is typical for improper layer bonding defects [45, 46]. With irregular surface defects, the Authors refer to those defects whose origin is not clear, but that mainly form during the removal of the supporting structures in horizontally built specimens or to subsurface defects revealed by the manual polishing. It is worth noting that more detailed classifications can be found in the literature [45]. However, the analysis of the effect of defects on the VHCF response carried out in the following Sections does not depend on the classification considered, since the defect size is the most influencing parameter, according to [23].

Critical defects on the fracture surfaces are representative of the defects that control the fatigue response. It is worth noting that images of defects obtained on polished sections would probably more clearly show the characteristic of each type of defect. However, rare and large defects, i.e., those that originate the fatigue cracks and that, accordingly, control the fatigue response, can be hardly found on polished surfaces and can be only revealed through fatigue tests. Moreover, representative images of defects on the fracture surfaces are more effective to show the critical defects. On the other hand, defects found on polished samples may not be representative of the characteristics of the critical defects.

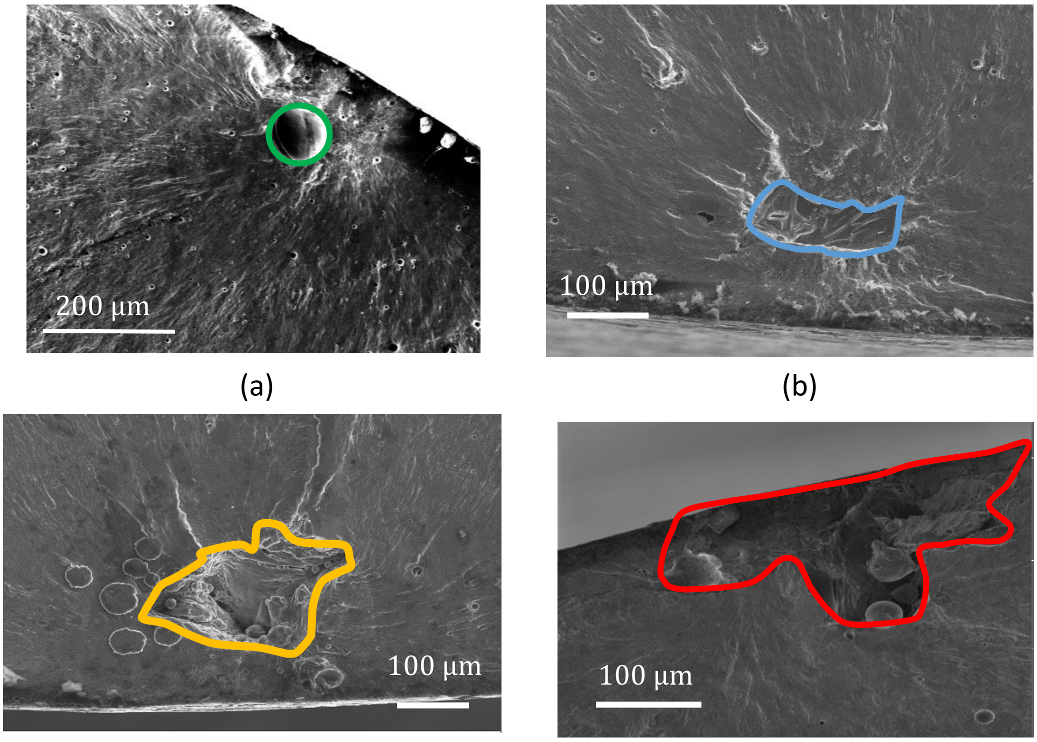

(a) (b)

(c) (d)

Figure 7: Types of critical defects: a) pore; b) Improper layer bonding (ILB) defect; c) defect due to incomplete fusion (IF); d) irregular surface defect (Irregular SD).

Fig. 8 compares the frequency of occurrence (Fig. 8a) and the size (Fig. 8b) of the different types of defects. For defects with an irregular shape, the guidelines reported in [23] have been followed to assess an equivalent defect size, $\sqrt{a_c}$.

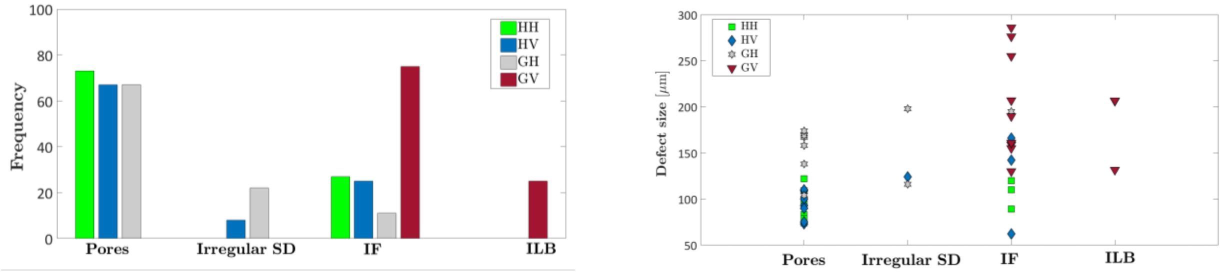

(a) (b)

Figure 8: Defect analysis: a) frequency of occurrence; b) size of the critical defect subdivided for type and tested specimen.

According to Fig 8a, for the HH, HV and GH specimens, the pores are the most critical defects, with a frequency of occurrence close to 70%; whereas, for the GV specimens, IF defects occur more frequently (about 70%). For the horizontally built specimens, pores are the most critical defects regardless of the tested volume. These pores mainly formed in the weak region where support structures were removed, and, accordingly, a size-effect correlated to the defect type was not observed. However, according to Fig. 8b, a size-effect correlated to the defect size is clear, as will be discussed in the following. A concentration of failures in the region where supporting structures are removed demonstrates that this is the weakest region within the risk-volume. Indeed, even if defects are present in other regions of material, they are surely not critical. A defect becomes critical depending on its size, on the stress distribution and on the local material properties. Since pores concentrated in the region where supporting structures are removed are at the origin of the fatigue failures in almost all horizontally built specimens, it can be inferred that these pores are the most critical defects for the specimens built in the horizontal direction.

On the other hand, the critical defect type switches from pores for small volumes to IF defects for the large Gaussian specimens in vertically built specimens. For justifying this behavior, Fig. 6b should be considered. Indeed, for vertically built specimens, a weaker region is not present within the cross-section. The critical defect size increases with the risk-volume (garnet red markers of GV specimens are above the blue diamond markers of HV specimens) due to size-effect. Generally, according to literature results [47, 48], IF defects and irregular defects are larger than pores. Since the probability of finding of large defects increases with the risk-volume, it is more likely that these defects are IF defects. This does not mean that pores do not form in large risk-volumes: indeed, large pores were also found on the fracture surface of GV specimens, but they did not become critical due to their smaller size or to their location within the risk-volume (internal defects are less critical than surface defects, according to [23]). Fig. 9 shows an example of a fracture surface of a GV specimen with non-critical pores and a large critical IF defect from which the fatigue crack originates.

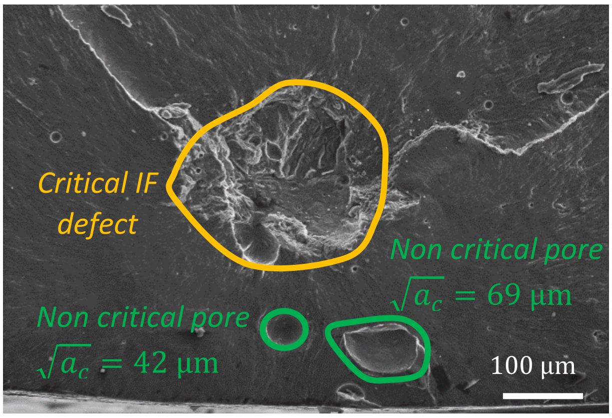

Figure 9: Fracture surface of a GV specimen showing a critical IF defect and two non-critical pores with smaller size.

Fig. 9 confirms that large pores can be also present in GV specimens, but they did not originate the fatigue crack due to their smaller size. The size of pores present in the Fig. 7 ($\sqrt{a_c} = 42\ \mu\mathrm{m}$ and $\sqrt{a_c} = 69\ \mu\mathrm{m}$) is close to the range for pore size found for HV specimens (Fig. 7b). This confirms that IF defects become the most critical defects in GV due to the risk-volume increment. Very large IF defects could be also found in HV specimens, but this is unlikely, and a larger number of specimens should be tested to find the same defect population.

In order to more properly assess the size-effect associated with the defect size, $\sqrt{a_c}$ is assumed to follow the Largest Extreme Value Distribution (LEVD), with cumulative distribution function (cdf), $F_{\sqrt{A_{d,0}}}$. The experimental data and the estimated $F_{\sqrt{A_{d,0}}}$ are shown in Fig. 10 (Fig. 10a for horizontally built specimens and Fig. 10b for vertically built specimens).

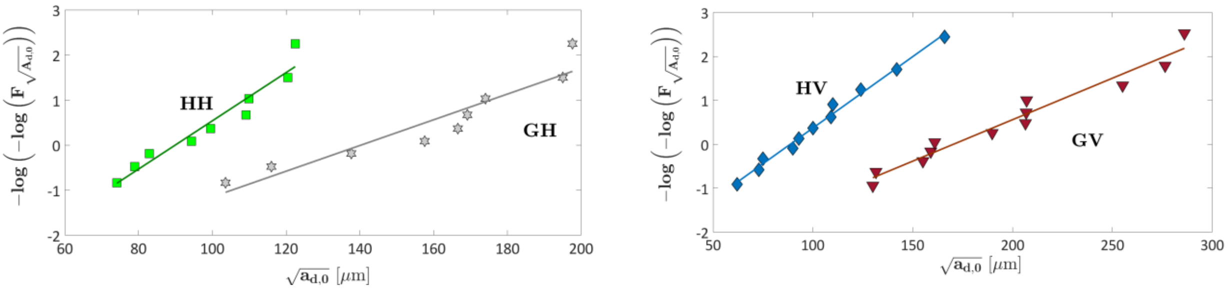

(a) (b)

Figure 10: Critical defect size and estimated LEVD on a Gumbel plot: specimens built in horizontal direction; specimens built in vertical direction.

The Gumbel plots in Fig. 10 highlight the size-effect associated to $\sqrt{a_c}$, regardless of the defect type. The critical defects in Gaussian specimens are significantly larger than the critical defects in hourglass specimens for both building directions. For the horizontally built specimens, 80% of the defects in Gaussian specimens are larger than the largest defect, $\sqrt{a_c}_{max}$, in hourglass specimens. Moreover, $\sqrt{a_c}_{max}$ in HH is about the 60% of the $\sqrt{a_c}_{max}$ in GH. Similarly, for vertically built specimens 60% of the defects in Gaussian specimens are larger than the largest defect in hourglass specimens and $\sqrt{a_c}_{max}$ in HV is about the 60% of $\sqrt{a_c}_{max}$ in GV. However, for the specimens built in vertical direction, the increment of the largest defect between hourglass and Gaussian specimens (from $166\ \mu\mathrm{m}$ to $286\ \mu\mathrm{m}$) is larger than that found in horizontally built specimens (from $122\ \mu\mathrm{m}$ to $198\ \mu\mathrm{m}$). Size-effect is therefore relevant by considering the defect size for both the horizontal and vertical specimens.

Moreover, the building orientation influences the defect size. Indeed, defects in horizontally and vertically built specimens are averagely the same, but rare and large defects are more likely in vertically built specimens. For example, the largest defect in horizontally built hourglass specimens is about $122\ \mu\mathrm{m}$, whereas three defects are larger than $122\ \mu\mathrm{m}$ in vertically built specimens, with the largest defect with size equal to $166\ \mu\mathrm{m}$. Similarly, in horizontally built Gaussian specimens all the critical defects found experimentally were characterized by an equivalent size smaller than $200\ \mu\mathrm{m}$, whereas for Gaussian vertically built specimens four larger defects with equivalent size up to $290\ \mu\mathrm{m}$ were experimentally found. The influence on the VHCF response of the anisotropy associated to the defect size is investigated in a statistical framework in Section 3.4.

3.4. Size-effects on the VHCF strength

In this section the influence of the specimen volume on the VHCF response is investigated by comparing the VHCF strengths. In order to account for the influence of the statistical distribution of $\sqrt{a_c}$ on the fatigue response, the marginal P-S-N curves, defined according to [49], are compared:

$$F_Y(y;x) = \int_0^\infty F_{Y|\sqrt{a_c}}(y;x;\ \sqrt{a_c}) f_{\sqrt{a_c}}(\sqrt{a_c}) d\sqrt{a_c}, \tag{1}$$

where $F_Y(y;x)$ is the cdf of y, being $y = \log_{10}(N_f)$ and $x = \log_{10}(s_{local})$, $F_{Y|\sqrt{a_c}}(y;x;\sqrt{a_c})$ is the cdf of the conditional distribution of the fatigue life (i.e., normally distributed and with mean dependent on x and $\sqrt{a_c}$) and $f_{\sqrt{a_c}}(\sqrt{a_c})$ is the probability density function (pdf) of LEVD for $\sqrt{a_c}$, according to Section 3.3. The model has been validated by the Authors in [25, 27]. Fig. 11 shows the estimated median and 0.1% P-S-N curves for specimens built in horizontal direction (Fig. 11a) and in vertical direction (Fig. 11b).

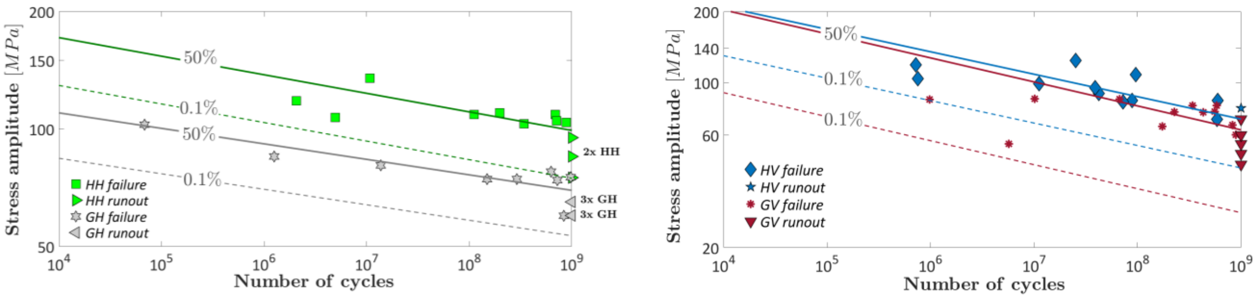

(a)

(b)

Figure 11: Median and 0.1% P-S-N curves for the tested specimens: a) horizontal building direction; b) vertical building direction.

According to Fig. 11a, size-effect is relevant for horizontally built specimens. The slopes of the two P-S-N curves are similar, being slightly larger for HH. However, the median and the 0.1% P-S-N curves for the HH are above the corresponding curves for the GH: the increment of $\sqrt{a_c}$ with the V_{90} has a significant effect on the VHCF response. The difference at 10^9 cycles is about 30% by considering the median VHCF strength and about the same (28%) by considering the 0.1% VHCF strength, since the scatter of the P-S-N curves for the HH and the GH data is similar. For the vertically built specimens, the median P-S-N curve for the hourglass specimens is above that for Gaussian specimens, but the difference is smaller (about 10% for the VHCF strength at 10^9 cycles). On the contrary, the percentage difference increases by comparing the 0.1% VHCF strength, being about 35%. Therefore, even if the median VHCF strength difference is smaller than that of horizontally built specimens, size-effect is also relevant for vertically built specimens. This is mainly associated to the range of the defect size which increases with the risk-volume and thus affects the VHCF response.

The comparison of the P-S-N curves and of the VHCF strengths highlighted the importance of taking into account the scatter associated with the VHCF strength in the analysis. For a proper statistical assessment, the VHCF strength at 10^9 cycles for each failure was statistically estimated. Indeed, in a statistical framework, for each i-th specimen failed at $N_{f,i}$ and at $s_{local,i}$, the quantile $\alpha_{th,i}$ of the fatigue life (or of the P-S-N curve that passes through) can be estimated. Given the $\alpha_{th,i}$ quantile, the corresponding VHCF strength at 10^9 cycles for the i-th specimen can be obtained by substituting $F_Y(y = 9; x) = \alpha_{th,i}$, and by solving Eq. (1) with respect to x. According to this procedure, it is possible to “shift” all the experimental failures to the corresponding experimental failure at 10^9 cycles. Fig. 12 shows, for each failure, the estimated VHCF strength at 10^9 cycles.

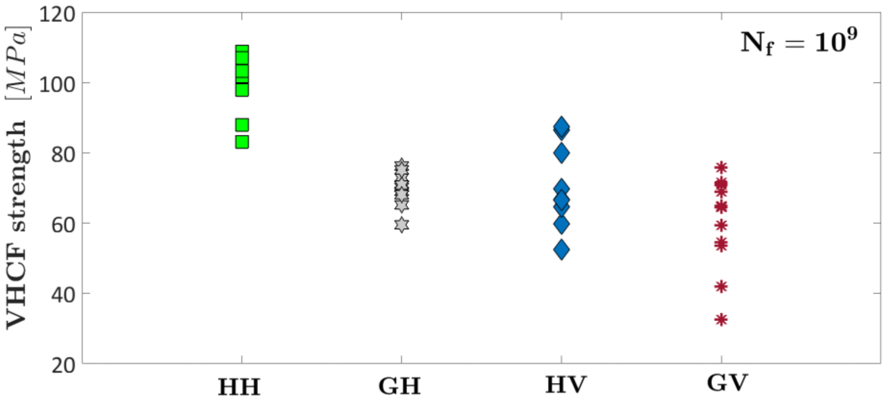

Figure 12: Estimated VHCF strengths at 10^9 cycles.

The Analysis of Variance (ANOVA) was employed to statistically compare the VHCF strengths at 10^9 cycles. In Table 3, the Sum of Squares (SS), the Degrees of Freedom (DOF), the Mean Squares (MS) and the estimated P-Values are reported. Two factors, volume and building orientation, and the possible interactions between them were considered in the analysis.

Table 3: ANOVA to investigate the effect of risk-volume (size-effect) and building orientation and the interaction between them on the VHCF response.

	SS	*DOF*	*MS*	*P-value*
Volume	3776	1	3776	**0.000**
Building orientation	3826	1	3825	**0.000**
Interaction	1020	1	1019	**0.003**
Error	3768	37	102	
Total	12062	40		

Table 3 further confirms that size-effect and building orientation significantly affect the VHCF response at 10^9 cycles. For both the volume and the building orientation factors, the P-value is close to 0. The ANOVA gives more strength to the results found by analyzing the P-S-N curves, since it permits to consider also the scatter associated to the fatigue response, which is large for AM parts. The interaction between the specimen size and the building orientation is statistically significant, as expected by considering Fig. 11 and Fig. 12.

These analyses confirm that size-effects significantly influence the VHCF response, pointing out the importance of experimentally verifying it when components are to be designed by considering the experimental results obtained through tests on specimens with small V_{90}.

3.5. Discussion

In this Section the experimental results are further analyzed, and the influence of the microstructure is also considered. According to Section 3.1, while for the horizontally built specimens the variation of the Vickers hardness among hourglass and Gaussian specimens is limited (it passes from $134\ \mathrm{HV}$ in GH to $128\ \mathrm{HV}$ in HH and is equal to $122\ \mathrm{HV}$ in the support region), for the vertically built specimens is larger, reducing from $146\ \mathrm{HV}$ in GH to $125\ \mathrm{HV}$ in HV. Since the process parameters were the same for all the specimens, the variation could be mainly due to the intrinsic scatter associated to the AM process, since many “hidden” factors could influence the final mechanical properties (e.g., the position of the specimens on the building platform). However, it should also be considered that, according to available literature [43, 50], thinner samples can exhibit lower hardness because of local heat accumulation taking place during processing, since the surrounding unmolten powder has lower heat dissipation capacity with respect to large bulk parts. This effect is probably superseded by the influence of building orientation in horizontal samples but becomes prominent in vertically built samples. Therefore, in the previous analysis this effect was not considered, since the scatter in the Vickers hardness can be considered as intrinsically associated with the manufacturing process. However, in order to exclude the influence of microstructure on the VHCF response and on size-effect, the experimental data for the vertically built specimens have been normalized by taking into account the Vickers hardness, according to [23]. Each experimental failure for HV has been multiplied by the ratio $\frac{(HV_{GV}+120)}{(HV_{HV}+120)}$, being HV_{HV} and HV_{GV} the Vickers hardness of HV and GV specimens, respectively. For the horizontally built specimen, the data have not been normalized, since the HV differences were small and, moreover, almost all the defects were in the area where support structures were removed, characterized by a similar Vickers hardness in HH and HG. Fig. 13 shows the experimental failures for HV and GV, normalized by the ratio $\frac{(HV_{GV}+120)}{(HV_{HV}+120)}$ and the estimated median and 0.1% P-S-N curve. The grey diamond markers are the original experimental data. It is worth noting that the data for the GV specimens have been normalized by the factor $\frac{(HV_{GV}+120)}{(HV_{HV}+120)}$ to better isolate the influence of defect size on the VHCF response and, accordingly, to more properly assess how size-effect related to the defect size affects the VHCF response. Indeed, according to [51], the Vickers hardness, correlated to the microstructure, influences the VHCF response. With the proposed normalization, according to [23], the dependency of the VHCF response on the microstructure can be eliminated, to more properly assess the influence of defects and size-effect.

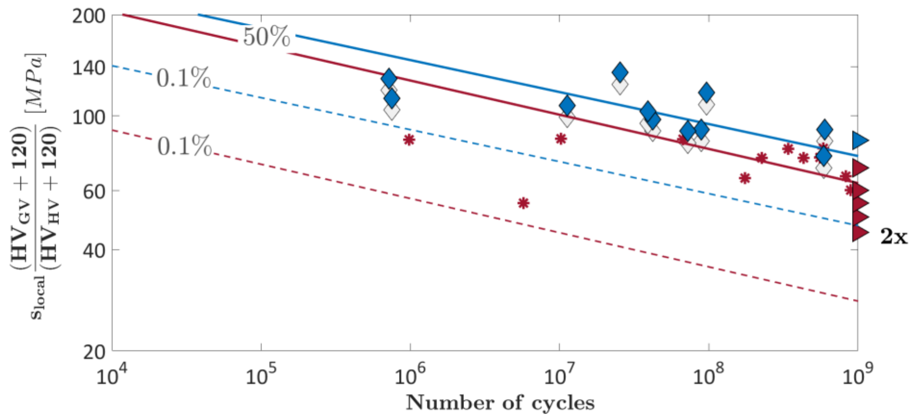

Figure 13: Median and 0.1% P-S-N curves estimated by normalizing the HV experimental data.

According to Fig. 13, the differences between the curves increase, with a 17% reduction by considering the median VHCF strength at 10^9 cycles and a 40% reduction by considering the 0.1% VHCF strength at 10^9 cycles, pointing out that, for vertically built specimens, the hardness difference partially hid the size-effect. Moreover, by repeating the ANOVA analysis with the normalized data, the interaction between the specimen size and the building orientation was found to be not statistically significant with a significance level of 1% (P-value equal to 3.5%).

The experimental results on size-effect can be also compared to the results obtained in the literature by testing specimens obtained through traditional manufacturing processes. In particular, in [25], experimental tests on hourglass and Gaussian specimens with risk-volumes close to those investigated in the present paper were carried out on an unrefined H13 steel and on a refined H13 steel subjected to an ESR process. Specimens were tested up to 10^{10} cycles and the marginal P-S-N curves were estimated by considering, for the VHCF region, a linear decreasing trend and a fatigue limit. All the fatigue failures originated from defects, mainly inclusions, randomly dispersed within the risk-volume. Table 4 compares the percentage decrement of the VHCF strength between the hourglass and Gaussian specimens at the runout number of cycles (i.e., 10^9 cycles in the present paper and 10^{10} cycles in [25]). The decrement was computed with respect to the VHCF strength of hourglass specimens estimated from the marginal P-S-N curves. The aim of this analysis is to qualitatively verify if size-effect on the VHCF response of traditionally built specimens and of AMed specimens with similar risk-volume have the same influence. It is worth noting that the comparison should be carried out by considering the experimental results on SLM AlSi10Mg specimens produced with traditional processes, but there are no available data in the literature. In [52, 53], the size-effect on the VHCF response of Al alloy specimens has been investigated by testing specimens with increasing diameter, but with risk-volumes different from those tested in the present paper. Therefore, a proper comparison cannot be carried out, since the risk-volume is a fundamental parameter. Moreover, the assessment of size-effects on the VHCF response of AMed AlSi10Mg specimens by analyzing literature data would be difficult, especially if the specimens are not produced with the same process parameters. Indeed, different process parameters can partially hide the size-effect and therefore do not permit to properly assess the real influence of the risk-volume on the VHCF response.

Table 4: Size-effect on the VHCF response: traditionally built specimens [25] and AM specimens (present paper).

VHCF strength at the runout number of cycles		
Quantile	50%	0.1%
H13 no ESR [25]	16%	23%
H13 ESR [25]	7%	8%
AlSi10Mg horizontal	30%	28%
AlSi10Mg vertical	17%	40%

According to Table 4, size-effect in AM has a larger influence. Indeed, for traditionally built specimens the decrement of the VHCF response due to size-effect is in the range [7-16]% by considering the median VHCF strength and in the range [8-23]% for the 0.1% VHCF strength. The decrement is larger for the unrefined steel (up to 23%), characterized by larger defects. On the other hand, the ranges are larger for the SLM AlSi10Mg specimens tested in the present paper, being [17-30]% by considering the median VHCF strength and [28-40]% for the 0.1% VHCF strength. The main reason is the larger increment of $\sqrt{a_c}$ with the risk-volume: the increment of the median defect size is smaller than 10 μm in [25], whereas it is larger than 50 μm for the tested AlSi10Mg specimens.

If the data on traditionally built Al alloys hourglass specimens with increasing diameter up to 12 mm are considered [52, 53], the VHCF strength decrement at 10^9 cycles is smaller than 20%. This support the evidence that size-effects in AMed parts tend to be larger, even if experimental tests on traditionally built specimens made of the same alloy and with the risk-volumes tested in the present paper are necessary to prove this.

This further analysis warns against the risk of designing components by considering the experimental VHCF results on TB specimens. The estimation of the effect of different factors, like size-effect, by considering literature results on TB specimens could have serious consequences on the structural integrity of the components, as proved in the present paper.

4. CONCUSIONS

In the paper, the influence of size-effects on the VHCF response of AlSi10Mg specimens produced through the SLM process was experimentally investigated. Hourglass specimens, with a risk-volume of $250\ \mathrm{mm}^3$, and Gaussian specimens, with a significantly larger risk-volume of $2330\ \mathrm{mm}^3$, were subjected to ultrasonic fully reversed tension-compression tests. Hourglass and Gaussian specimens were produced in horizontal and in vertical direction and tested in the as-built condition after a manual mechanical polishing. The specimens were tested up to failure or up to 10^9 cycles and manufacturing defects were the cause of all the VHCF failures. The following conclusions can be drawn:

1) Horizontally built specimens show a Vickers hardness reduction close to the region where support structures were removed. This behavior was found both in hourglass and Gaussian specimens: the support region therefore represents a weaker region for horizontally built specimens. On the other hand, for vertically built specimens, the Vickers hardness was found to be uniform within the cross-section.
2) Defects originating the fatigue failures (critical defects) were concentrated close to the surface for all the tested specimens. In particular, for horizontally built specimens, they were

concentrated in the region where support structures were removed (largest distance from the surface smaller than $500\ \mu\mathrm{m}$). No difference between hourglass and Gaussian specimens was found. For vertically built specimens, critical defects were concentrated close to the surface, but for Gaussian specimens 3 defects were farther from the surface (up to $1.5\ \mathrm{mm}$ from the surface). The larger dispersion in vertical Gaussian specimens is related to the larger tested volume, since, in vertically built specimens, weaker regions were not present, like in the horizontal specimens (i.e. support region).

3) The most critical defects in horizontally built specimens were pores, being at the origin of the critical fatigue crack in about the 70% of the fatigue failures. No size-effect correlated to the type of defect was found and the main reason is that all the fatigue failures originated in the weaker supports region where large pores were found to be more frequent. On the contrary, for specimens built in vertical direction, the most critical defects were pores in hourglass specimens, whereas became incomplete fusion defects in larger Gaussian specimens. The main reason is the increment of the tested volume: indeed, rare incomplete fusion defects, generally larger than pores, are less probable in the small volume of hourglass specimens.
4) A significant size-effect associated with the defect size was experimentally found. The largest defect in hourglass specimens was found to be about the 60% of the largest defect in the corresponding Gaussian specimen for both building orientations.
5) The VHCF strength decrement was significant due to size-effect. For both building orientations, the curves for the hourglass specimens were above the curves for the Gaussian specimens. For the horizontally built specimens, the VHCF strength decrement was about 30% for the median and 0.1% VHCF strength at 10^9 cycles. On the other hand, for vertically built specimens the decrement was smaller for the median VHCF strength at 10^9 cycles,

about 15%, and larger for the 0.1% VHCF strength at 10^9 cycles, about 40%. The reason is the larger range of the defect size in Gaussian vertically built specimens, which affects the VHCF response. These results highlight the importance of properly assessing and accounting for the scatter associated with the VHCF strength when the effect of different factors on the fatigue response is investigated.

6) Size-effect in AM was compared to the size-effect found in the literature by testing specimens made of two high strength steels (H13 steel) with similar risk-volume and produced with traditional processes. For the latter, the decrement was found in the range $[7\text{-}16]\%$ by considering the median VHCF strength and in the range $[8\text{-}23]\%$, significantly smaller than the range found for the tested AlSi10Mg SLM specimens.

The experimental results in the paper confirm the importance of properly taking into account size-effects when components are to be designed, especially if produced through AM process, for which it has a stronger influence. Furthermore, size-effects, as well as other factors (e.g., the building orientation), should be properly verified for AM parts to guarantee their structural integrity: AM components cannot be safely designed by relying on literature results obtained by testing TB specimens.

REFERENCES

[1] Kusoglu IM, Gökce B, Barcikowski S. Research trends in laser powder bed fusion of Al alloys within the last decade. Addit Manuf 2020;36:101489. https://doi.org/10.1016/j.addma.2020.101489 .

[2 Huang SH, Liu P, Mokasdar A, Hou L Additive manufacturing and its societal impact: a literature review. Int J Adv Manuf Technol 2013; 67:1191–1203. https://doi.org/10.1007/s00170-012-4558-5

[3] Bandyopadhyay A, Traxe KD Invited review article: Metal-additive manufacturing—Modeling strategies for application-optimized designs. Additive Manufacturing 2018; 22; 758-774. https://doi.org/10.1016/j.addma.2018.06.024

[4] Brackett D, Ashcroft I, Hague R, Topology optimization for additive manufacturing, Solid Free. Fabr. Symp. 2011; 348: 362

[5] Lewandowski JJ, Seifi M. Metal Additive Manufacturing: A Review of Mechanical Properties. Annual Review of Materials Research 2016; 46: 151-186. https://doi.org/10.1146/annurev-matsci-070115-032024

[6] Gorelik M. Additive manufacturing in the context of structural integrity. . Int J Fatigue 2017; 94 (2): 168-177. https://doi.org/10.1016/j.ijfatigue.2016.07.005

[7] Song B, Zhao X, Li S, Han C, Wei Q, Wen S, Liu J, Shi Y. Differences in microstructure and properties between selective laser melting and traditional manufacturing for fabrication of metal parts: A review. Front. Mech. Eng. 2015; 10: 111–125. https://doi.org/10.1007/s11465-015-0341-2

[8] Brusa E, Sesana R, Ossola E. Numerical modeling and testing of mechanical behavior of AM Titanium alloy bracket for aerospace applications. Procedia Struct Integr 2017; 5: 753–60. https://doi.org/10.1016/j.prostr.2017.07.166

[9] Plocher J, Panesar A. Review on design and structural optimisation in additive manufacturing: Towards next-generation lightweight structures. Mater Des 2019; 183. https://doi.org/10.1016/j.matdes.2019.108164.

[10] Kok Y, Tan XP, Wang P, Nai MLS, Loh NH, Liu E, Tor SB. Anisotropy and heterogeneity of microstructure and mechanical properties in metal additive manufacturing: A critical review. Mater. Des 2018; 139: 565-586. https://doi.org/10.1016/j.matdes.2017.11.021

[11] Herzog D, Seyda V, Wycisk E, Emmelmann C. Additive manufacturing of metals. Acta Mater. 2016; 117: 371-392. 10.1016/j.actamat.2016.07.019

[12] Gong X, Anderson T, Chou K. Review on powder-based electron beam additive manufacturing technology. Manuf. Rev. 2014, 1: 2-14. https://doi.org/10.1051/mfreview/2014001

[13] Khorasani AM, Gibson I, Ghaderi A, Mohammed MI. Investigation on the effect of heat treatment and process parameters on the tensile behaviour of SLM Ti-6Al-4V parts. Int J Adv Manuf Technol 2019; 101: 3183–3197. https://doi.org/10.1007/s00170-018-3162-8

[14] https://www.eos.info/case_studies/additive-manufacturing-of-antenna-bracket-for-satellite, Accessed 22th October 2020

[15] Thompson SM, Aspina ZS, Shamsaei N, Elwany A; Bian L. Additive manufacturing of heat exchangers: A case study on a multi-layered Ti–6Al–4V oscillating heat pipe. Additive Manufacturing 2015; 8: 163-174. https://doi.org/10.1016/j.addma.2015.09.003

[16] Khorasani AM, Gibson I, Goldberg M, Littlefair G. A survey on mechanisms and critical parameters on solidification of selective laser melting during fabrication of Ti-6Al-4V prosthetic acetabular cup. Mater Design 2016; 103: 348-355. https://doi.org/10.1016/j.matdes.2016.04.074

[17] Yadollahi A, Shamsaei N. Additive manufacturing of fatigue resistant materials: Challenges and opportunities. Int. J. Fatigue 2017; 98: 14-31. https://doi.org/10.1016/j.ijfatigue.2017.01.001

[18] Molaei R, Fatemi A. Fatigue Design with Additive Manufactured Metals: Issues to Consider and Perspective for Future Research. Procedia Eng. 2018; 213. 5-16. https://doi.org/10.1016/j.proeng.2018.02.002

[19] Sanae N, Fatemi A. Defects in additive manufactured metals and their effect on fatigue performance: A state-of-the-art review. Prog. Mater. Sci (In press). https://doi.org/10.1016/j.pmatsci.2020.100724

[20] Beretta S, Romano S. A comparison of fatigue strength sensitivity to defects for materials manufactured by AM or traditional processes. Int J Fatigue 2017; 94: 178-191. doi.org/10.1016/j.ijfatigue.2016.06.020

[21] Siddique S, Imran M, Rauer M, Kaloudis M, Wycisk E, Emmelmann C, Walther F. Computed tomography for characterization of fatigue performance of selective laser melted parts . Mater Design 2015; 83: 661-669. https://doi.org/10.1016/j.matdes.2015.06.063

[22] Best JP, Ostergaard HE, Li B, Stolpe M, Yang F, Nomoto K, Hasib MB, Muránsky O, Busch R, Li X, Kruzic JJ. Fracture and fatigue behaviour of a laser additive manufactured Zr-based bulk metallic glass. Additive Manufaturing 2020; 36. https://doi.org/10.1016/j.addma.2020.101416

[23] Murakami Y. Metal Fatigue: Effects Of Small Defects And Nonmetallic Inclusions. 1st ed. Oxford: Elsevier Ltd; 2002.

[24] Furuya Y. Notable size effects on very high cycle fatigue properties of high strength steel. Mater. Sci. Eng. A 2011; 528: 5234–5240. https://doi.org/10.1016/j.msea.2011.03.082

[25] Tridello, A. VHCF Response of Two AISI H13 Steels: Effect of Manufacturing Process and Size-Effect. Metals 2019, 9(2), 133; https://doi.org/10.3390/met9020133

[26] Paolino DS, Tridello A, Chiandussi G, Rossetto M. On specimen design for size effect evaluation in ultrasonic gigacycle fatigue testing. Fatigue Fract Engng Mater Struct 2014; 37: 570–579. doi.org/10.1111/ffe.12149

[27] Tridello A, Biffi CA, Fiocchi J, Bassani P, Chiandussi G, Rossetto M, Tuissi A, Paolino DS. VHCF response of as-built SLM AlSi10Mg specimens with large loaded volume. Fatigue Fract. Engng. Mater. Struct. 2018; 41: 1918–1928. doi.org/10.1111/ffe.12830

[28] Paolino DS, Tridello A, Fiocchi J, Biffi CA, Chiandussi G, Rossetto M, Tuissi A. VHCF Response up to 10^9 Cycles of SLM AlSi10Mg Specimens Built in a Vertical Direction. Appl. Sci. 2019; 9: 2954-2967. doi.org/10.3390/app9152954

[29] Bathias C, Paris PC. Gigacycle fatigue in mechanical practice. 2nd ed. New York: CRC Dekker; 2005.

[30] Tridello A, Paolino DS, Chiandussi G, Rossetto M. Comparison between dog-bone and Gaussian specimens for size effect evaluation in gigacycle fatigue. Frattura e Integrità Strutturale 2013; 26: 49–56. https://doi.org/10.3221/IGF-ESIS.26.06

[31] ASTM Standard E1876-09 (2009). Standard test method for dynamic Young’s modulus, Shear modulus, and Poisson’s ratio by impulse excitation of vibration. West Conshohocken (PA): ASTM International; 2009.

[32] Brandl E, Heckenberger U, Holzinger V, Buchbinder D, Additive manufactured AlSi10Mg samples using Selective Laser Melting (SLM): Microstructure, high cycle fatigue, and fracture behavior, Materials & Design 2012, 34, 159-169.https://doi.org/10.1016/j.matdes.2011.07.067.

[33] Croccolo D, De Agostinis M, Fini S, Olmi G, Bogojevic N, Ciric-Kostic S. Effects of build orientation and thickness of allowance on the fatigue behaviour of 15–5 PH stainless steel manufactured by DMLS. Fatigue Fract. Engng. Mater. Struct. 2018; 41: 900–916.[34] Sohar CR, Betzwar-Kotas A, Gierl C, Weiss B, Danninger H. Gigacycle fatigue behavior of a high chromium alloyed cold work tool steel. Int J Fatigue 2008; 30 (7): 1137-1149. https://doi.org/10.1016/j.ijfatigue.2007.09.012

[35] Furuya Y, Takeuchi E. Gigacycle fatigue properties of Ti–6Al–4V alloy under tensile mean stress. Mater Sci Eng A 2014; 598: 135–140. https://doi.org/10.1016/j.msea.2014.01.019

[36] Tridello A, Paolino DS, Chiandussi G, Rossetto M. Gaussian specimens for VHCF tests: Analytical prediction of damping effects Int. J. Fatigue. 2016; 83: 36-41. https://doi.org/10.1016/j.ijfatigue.2015.04.025

[37] Maeshima T, Oh-ishi K. Solute clustering and supersaturated solid solution of AlSi10Mg alloy fabricated by selective laser melting. Heliyon 2019; 5 :e01186. https://doi.org/10.1016/j.heliyon.2019.e01186.

[38] Biffi CA, Fiocchi J, Bassani P, Paolino DS, Tridello A, Chiandussi G, Rossetto M, Tuissi A. Microstructure and preliminary fatigue analysis on AlSi10Mg samples manufactured by SLM. Procedia Structural Integrity 2017; 7: 50-57. https://doi.org/10.1016/j.prostr.2017.11.060

[39] Zhang J, Song B, Wei Q, Bourell D, Shi Y. A review of selective laser melting of aluminum alloys: Processing, microstructure, property and developing trends, Journal of Materials Science & Technology, 35, 270–84 (2019).

[40] Mower TM, Long MJ. Mechanical behavior of additive manufactured, powder-bed laser-fused materials. Materials Science & Engineering A 2016; 651: 198-213.

[41] Bagherifard S, Beretta N, Monti S, Riccio M, Bandini M, Guagliano M. On the fatigue strength enhancement of additive manufactured AlSi10Mg parts by mechanical and thermal post-processing. Materials and Design 2018; 145: 28-41.

[42] Q. Cao, Y. Bai, J. Zhang, Z. Shi, J.Y.H. Fuh, H. Wang, Removability of 316L stainless steel cone and block support structures fabricated by Selective Laser Melting (SLM), Mater. Des. 191 (2020) 108691. doi:10.1016/j.matdes.2020.108691.[43] Yuan L, Gu D, Lin K, Ge Q, Shi X, Wang H, et al. Influence of structural features on processability, microstructures, chemical compositions, and hardness of selective laser melted complex thin-walled components. Int J Adv Manuf Technol 2020; 109: 1643–54. https://doi.org/10.1007/s00170-020-05773-1. [44] Tang M, Pistorius C. Oxides, porosity and fatigue performance of AlSi10Mg parts produced by selective laser melting. Int J Fatigue 2017; 94 (2): 192-201. doi.org/10.1016/j.ijfatigue.2016.06.002

[45] Sanaei N, Fatemi A. Defects in additive manufactured metals and their effect on fatigue performance: A state-of-the-art review. Prog Mater Sci 2021;117:100724. https://doi.org/10.1016/j.pmatsci.2020.100724.

[46] Zhang B, Li Y, Bai Q, Defect Formation Mechanisms in Selective Laser Melting: a Review. Chinese J Mech Eng 2017; 30: 515–527. https://doi.org/10.1007/s10033-017-0184-3.

[47] Gong H, Rafi K, Gu H, Janaki Ram GD, Starr T, Stucker B. Influence of defects on mechanical properties of Ti–6Al–4 V components produced by selective laser melting and electron beam melting. Mater Design 2015; 86: 545-555. https://doi.org/10.1016/j.matdes.2015.07.147

[48] du Plessis A, Yadroitsava I, Yadroitsev I. Effects of defects on mechanical properties in metal additive manufacturing: A review focusing on X-ray tomography insights. Mater Design 2020; 187. https://doi.org/10.1016/j.matdes.2019.108385

[49] Paolino DS, Tridello A, Chiandussi G, Rossetto M. S-N curves in the very-high-cycle fatigue regime: statistical modeling based on the hydrogen embrittlement consideration. Fatigue Fract. Eng. Mater. Struct. 2016; 39: 1319-1336. https://doi.org/10.1111/ffe.12431

[50] Majeed A, Ahmed A, Liu B, Ren S, Yang J. Influence of wall thickness on the hardness of AlSi10Mg alloy parts manufactured by selective laser melting. Procedia CIRP 2019; 81: 459–63. https://doi.org/10.1016/j.procir.2019.03.079 .

[51] Tridello A, Fiocchi J, Biffi CA, Chiandussi G, Rossetto M, Tuissi A, et al. Effect of microstructure, residual stresses and building orientation on the fatigue response up to 10^9 cycles of an SLM AlSi10Mg alloy. Int J Fatigue 2020;137:105659. https://doi.org/10.1016/j.ijfatigue.2020.105659.

[52] Xue H, Sun Z, Zhang X, Gao T, Li Z. Very High Cycle Fatigue of a Cast Aluminum Alloy: Size Effect and Crack Initiation. JMEPEG 2018; 27: 5406–5416.

[53] Invernizi AS Invernizzi, S.; Montagnoli, F.; Carpinteri, A. Experimental Evidence of Specimen-Size Effects on EN-AW6082 Aluminum Alloy in VHCF Regime. Appl. Sci. 2021, 11, 4272. https://doi.org/10.3390/app11094272